



THE UNIVERSITY *of* EDINBURGH

Edinburgh Research Explorer

Interfacial adsorption kinetics of methane in microporous kerogen

Citation for published version:

Wang, R, Datta, S, Li, J, Alafnan, SFK, Gibelli, L & Borg, MK 2023, 'Interfacial adsorption kinetics of methane in microporous kerogen', *Langmuir*, vol. 39, no. 10, pp. 3742-3751.
<https://doi.org/10.1021/acs.langmuir.2c03485>

Digital Object Identifier (DOI):

[10.1021/acs.langmuir.2c03485](https://doi.org/10.1021/acs.langmuir.2c03485)

Link:

[Link to publication record in Edinburgh Research Explorer](#)

Document Version:

Peer reviewed version

Published In:

Langmuir

General rights

Copyright for the publications made accessible via the Edinburgh Research Explorer is retained by the author(s) and / or other copyright owners and it is a condition of accessing these publications that users recognise and abide by the legal requirements associated with these rights.

Take down policy

The University of Edinburgh has made every reasonable effort to ensure that Edinburgh Research Explorer content complies with UK legislation. If you believe that the public display of this file breaches copyright please contact openaccess@ed.ac.uk providing details, and we will remove access to the work immediately and investigate your claim.



Interfacial adsorption kinetics of methane in microporous kerogen

Runxi Wang,^{*,†} Saikat Datta,^{*,‡} Jun Li,^{*,¶} Saad F. K. Al-Afnan,^{*,¶} Livio Gibelli,^{*,‡}
and Matthew K. Borg^{*,‡}

[†]*Institute of New Energy and Low-carbon Technology, Sichuan University, Chengdu, 610065, China*

[‡]*School of Engineering, Institute of Multiscale Thermofluids, The University of Edinburgh, Edinburgh EH9 3FB, UK*

[¶]*Center for Integrative Petroleum Research, College of Petroleum Engineering and Geosciences, King Fahd University of Petroleum and Minerals, Dhahran 31261, Saudi Arabia*

E-mail: runxi.wang@scu.edu.cn; saikat.mech@gmail.com; lijun04@gmail.com;
safnan@kfupm.edu.sa; livio.gibelli@ed.ac.uk; matthew.borg@ed.ac.uk

Abstract

Rapid declines in unconventional shale production arise from the poorly understood interplay between gas transport and adsorption processes in microporous organic rock. Here, we use high-fidelity molecular dynamics (MD) simulations to resolve the time-varying adsorption of methane gas in realistic organic rock samples, known as kerogen. The kerogen samples derive from various geological shale fields, with porosities ranging between 20-50%. We propose a kinetics sorption model based on a generalised solution of diffusive transport inside a nanopore, to describe the adsorption kinetics in kerogen, which gives excellent fits with all our MD results, and we demonstrate it scales with the square of the length of kerogen. The MD adsorption time constants for all samples are compared with a simplified theoretical model, which we derive from the Langmuir isotherm for adsorption capacitance and the free-volume theory for steady, highly-confined bulk transport. While the agreement with the MD results is qualitatively very good, it reveals that in the limit of low porosity, the diffusive transport term dominates the characteristic time-

scale of adsorption, while the adsorption capacitance becomes important for higher pressures. This work provides the first data set for adsorption kinetics of methane in kerogen, a validated model to accurately describe this process, and a qualitative model that links adsorption capacitance and transport with the adsorption kinetics. Furthermore, this work paves the way to upscale interfacial adsorption processes to the next scale of gas transport simulations in mesopores and macropores of shale reservoirs.

Introduction

Compared with conventional gas fields, shale gas extraction is still not well predicted and understood.¹ Natural production of methane gas occurs through chemical-reaction processes inside the sedimentary rock called kerogen, which adsorbs inside the nanopores² owing to the intermolecular van der Waals forces. Adsorption is well known to depend on the formation pressure, temperature and the properties of the organic matter.³⁻⁶ In production, hydrofracking is often used to improve the connectivity of the ultra-low permeability pores inside the kerogen

matrix, which increases the mobility of the gas and the gas recovery.⁷ Despite turning to these intense stimulating techniques, the productivity of shale reservoirs has been often found to rapidly reduce with time during gas production, making forecasting of a reservoir unmanageable and unreliable.⁸ Understanding the kinetics sorption processes of methane at the interface of kerogen matter — i.e. the time-varying adsorption and desorption processes when subject to changes in local reservoir pressures — is foundational to solving the decline in extraction during shale gas production.

Experiments remain a useful part of understanding steady-state adsorption in nanopores and macropores of shale,⁹ including the impact of local porosity,¹⁰ measuring diffusion coefficients,¹¹ and the impact of temperature,¹² to name a few. However, experiments still have limitations in revealing clearly the physics of the local, dynamic transport and adsorption processes that occur at a molecular level, and free of heterogeneous effects. Furthermore, compared with a large number of adsorption models in the literature,^{9,13–15} theoretical frameworks accurately describing the time-varying transfer of gas at an interface of a porous rock, are still lacking.

Molecular dynamics (MD) simulation has unique advantages in that it can be used to study the gas transport inside nanopores with high spatial and temporal resolution. For example, using MD, the self-diffusion of hydrocarbons of varying chain length was directly measured in equilibrium simulations.^{16,17} Due to the extremely low permeability of kerogen, the transport of these hydrocarbon chains within the nanopores is found to be driven by self-diffusion, and importantly, Darcy’s law is found to no longer be valid.^{9,18–21} As the velocity cross-correlations of alkane molecules are no longer significant, the transport mechanisms are dominated by properties of the matrix and adsorbed fluid, which is in contrast to previous classical understanding, where viscosity and porosity dominate porous media flows.^{16,22} Other similar MD simulations were used to study methane displacement in carbon nanochannels,²³ oil migration in nanopores,

and methane adsorption/desorption from carbon nanotubes²⁴ and kerogen.^{25–27}

In this work, we use non-equilibrium molecular dynamics (NEMD) simulation to accurately measure the time-varying adsorption of methane gas molecules inside realistic organic rock samples. We derive a sorption kinetics model that best describes this adsorption process, and demonstrate it fits all our MD results well. From these fits, we are able to rationalise the adsorption process using the adsorption time constant for various sample maturities, porosities and reservoir pressures. We also use MD to validate the scaling law of the adsorption time constant, which relates to the square of the kerogen length, that arises from the sorption kinetics model. We believe the sorption kinetics model and the MD data generated for these samples will be useful when upscaling in meso/macro flow simulations,^{28–31} where boundary models of the sorption kinetics processes are currently missing. Finally, a simplified theoretical model for the adsorption time constant is developed, which we find linearly depends on the flow resistance and adsorption capacitance. This allows us to untangle the flow transport from the pore adsorption capacitance to understand their individual impact on the adsorption time constant, for the parametric space considered.

Materials and Methods

Molecular dynamics simulations

The time-varying adsorption of methane inside kerogen samples, which interface with a reservoir of given pressure P , is investigated using the NEMD set-up in Figure 1a. The system is periodic in the y and z directions, and non-periodic in the x direction. A kerogen sample is fixed on one end of the simulation domain and a piston is used on the other end of the domain to maintain a reservoir of methane molecules at a steady pressure, such that the direction of adsorption is in the negative x direction. The force applied on each piston atom is $F = PA/N$, where P is the target reser-

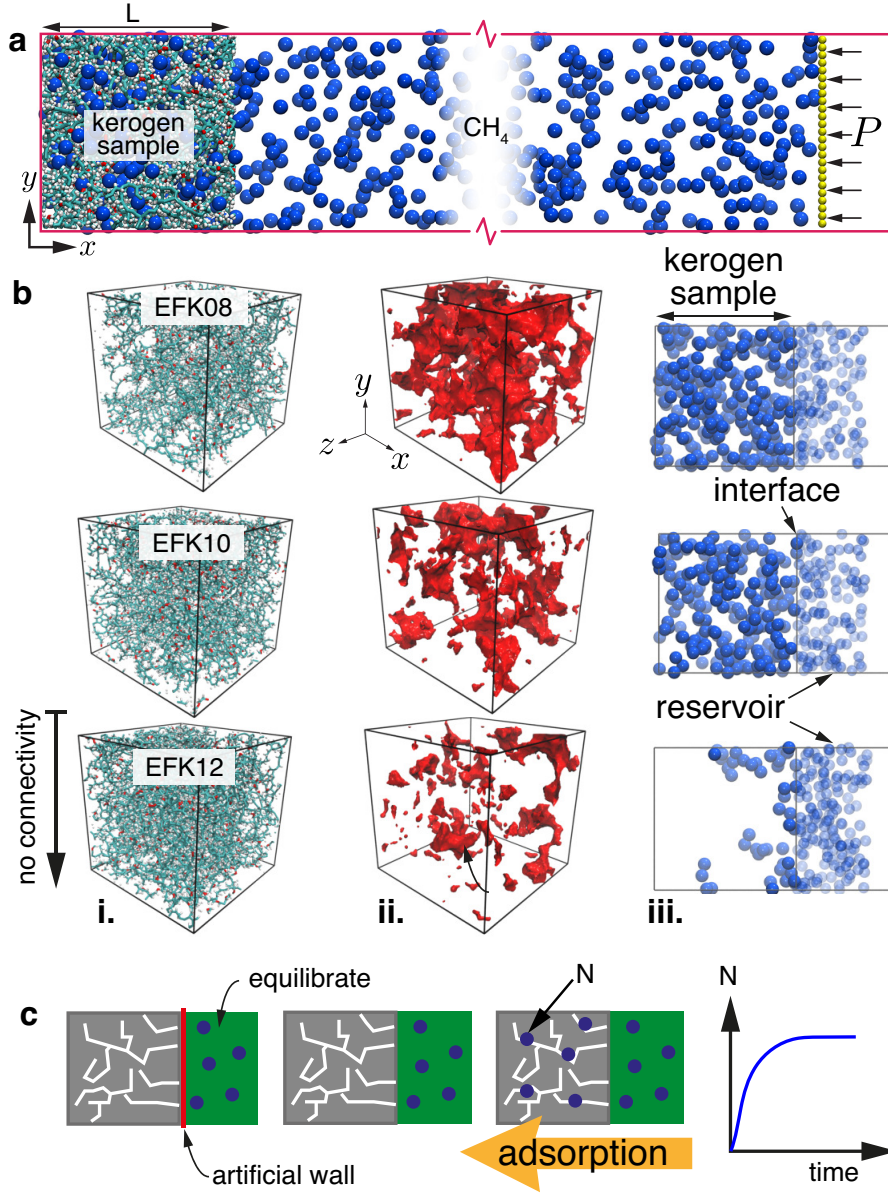


Figure 1: (a) Schematic of the NEMD set-up for the adsorption simulations used in this work. Kerogen of length L equal to the sample length $L_s = 50 \text{ \AA}$ shown on the left, methane (CH_4) molecules are coloured blue and the piston on the right is coloured yellow, which sets the reservoir pressure P . (b) i. EFK kerogen samples at three different densities 0.8 g/cm³ (EFK08), 1.0 g/cm³ (EFK10), and 1.2 g/cm³ (EFK12), ii. their respective pore space and iii. side view of steady-state methane molecule adsorption in the kerogen samples for a reservoir pressure 10 MPa; note that the kerogen is removed in ii. and iii. for better visualisation. (c) Procedure for initialising adsorption MD simulations. Here, the kerogen sample is drawn in grey, the temporary barrier used during reservoir gas equilibration is in red, and the reservoir is highlighted green; blue circles are the methane molecules.

voir pressure varying between 1–50 MPa, A is the piston cross-sectional area, and $N = 625$ is the number of piston atoms. The direction of the piston force always points into the reservoir, while the mass of the atoms on the piston are taken to be those of carbon.

State-of-the-art molecular structures of kerogen (sample size: $L_s^3 = 50 \times 50 \times 50 \text{ \AA}^3$) were obtained from Bousige et al.,³² which derive from the Middle East (MEK, Type II), Eagle Ford field (EFK, Type II) and the Marcellus field (MarK, Type IV) reservoirs. The densities vary between 0.8–1.4 g/cm³, which translate to porosities ($\phi = 20\text{--}60\%$).¹⁷ These kerogen samples are constructed by Bousige et al.³² using the hybrid reverse Monte Carlo reconstruction method, which match the C–C pair distribution functions, pore size distribution, elastic properties, adsorption and vibrational density of state with experiments. We find that samples with densities higher than ~ 1.0 g/cm³ do not have bulk connectivity (see Figure 1b for EFK12), and the adsorption will only be superficial at the interface. Therefore, in this work we focus only on samples that have bulk connectivity (i.e. 0.8 and 1.0 g/cm³ densities). The force fields between kerogen and methane are obtained from experimental calibrations of adsorption of the same kerogen samples,^{17,32} where methane is modelled as a single site Lennard-Jones molecule³³ (see Table 1 for all pair-potential combinations). Simulations are performed in the NVT ensemble using the MD software LAMMPS.³⁴ The temperature of methane in all simulations is maintained at 423 K (relevant to shale reservoirs at burial depth ~ 5 km) by the Nosé-Hoover thermostat³⁵ applied only in the non-flow (y and z) directions.

Kerogen structures have been treated either as *rigid* or *flexible* to compare their influence on the adsorption kinetics. The atoms of a rigid kerogen are fixed at their equilibrium position, while those of a flexible kerogen are modelled with a spring force (spring constant of 100 kcal/(mol \AA^2)) tethering them to their equilibrium position and each atom is connected to a Langevin thermostat set at the same target temperature of the reservoir. The simulations of rigid kerogen are conducted with a

Table 1: Lennard Jones pair-interaction parameters for energy ϵ_{ij} and lengthscale σ_{ij} between methane (CH_4) and other molecular species: kerogen (C,O,H) and piston (P). A potential cut-off of $r_{\text{cut}} = 20 \text{ \AA}$ is used, except for the pair-interaction kerogen atoms, which use an artificial small $r_{\text{cut}} = 0.1 \text{ \AA}$, since their thermal motion are dictated mostly by the Langevin thermostat.

Molecule pairs	ϵ_{ij} (Kcal/mol)	σ_{ij} (\AA)
$\text{CH}_4\text{-CH}_4$	0.2941	3.730
$\text{CH}_4\text{-C}$	0.12787	3.545
$\text{CH}_4\text{-O}$	0.21351	3.45
$\text{CH}_4\text{-H}$	0.09362	3.075
$\text{CH}_4\text{-P}$	0.005	2.5
C-C	0.0556	3.360
O-O	0.1550	3.170
H-H	0.0298	2.420

time-step of 2 fs, while the flexible model uses a smaller time-step of 0.5 fs. As we detail in the Supporting Information (SI) document, we have chosen the flexible kerogen structure in our study, as the rigid kerogen was found to create longer adsorption timescales τ (see Figure 2). In previous work,^{36,37} differences in gas self-diffusion between flexible and rigid kerogen models were observed to originate from a combination of swelling and tight flexible constrictions that open/close within the atomic matrix. In our case, our set-up does not handle swelling, and we find that an adiabatic treatment of the rigid kerogen matrix prevents the changes in heat formation in the adsorbing gas to rapidly thermalise within the kerogen, which lengthens the time of adsorption. This is resolved using a flexible and thermally constrained matrix. Figure 2 shows a comparison of the adsorption timescale τ with the corresponding thermal relaxation timescale τ_T of the gas during adsorption for both rigid and flexible treatments. For the rigid kerogen matrix, the thermal relaxation timescale is comparable to the adsorption timescale, while for the flexible matrix, the thermal relaxation timescale is much lower. Further details are given in the SI.

Since the kerogen structures are constructed in a periodic domain, we are also able to

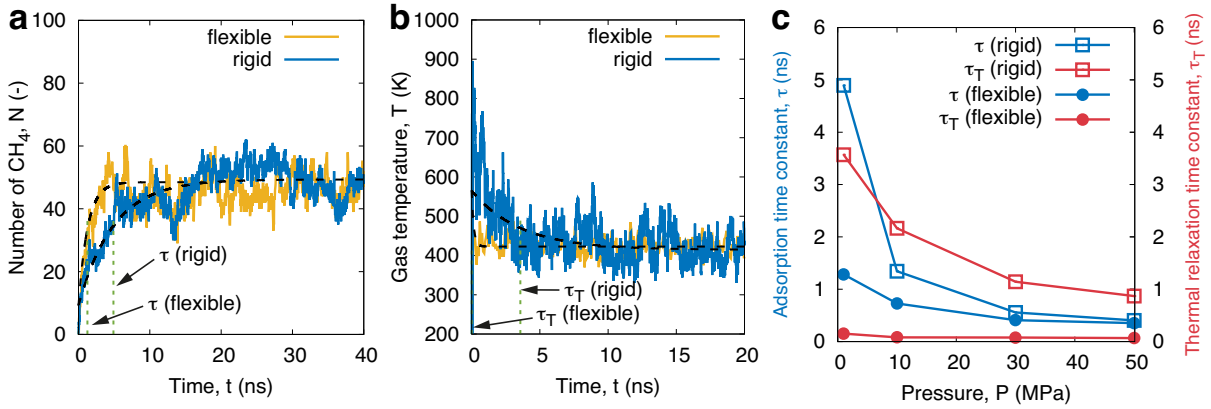


Figure 2: Differences in the (a) adsorption and (b) temperature of methane inside the EFK 0.8 g/cm³ sample at 1 MPa between rigid and flexible kerogen matrix models. (c) Comparison of the adsorption time constant (τ ; blue) with the thermal relaxation time constant (τ_T ; red).

place multiple equivalent samples side-by-side, to construct a thicker kerogen, given by $L = iL_s$, where $L_s = 50$ Å is the sample size, and $i = 1, 2, \dots$ is an integer representing the number of unit replicas.

The MD procedure is shown schematically in Figure 1c. In the initialisation step, the number of methane molecules set in the reservoir are generated at the target density and pressure, taken from NIST.³⁸ The equation of state has also been checked with independent MD simulations of methane as well as with the action of the piston. The size of the reservoir between piston and kerogen is chosen such that the number of methane molecules that remain in the reservoir after steady-state adsorption, remains >95%. Starting from an empty kerogen, the initialised methane molecules in the reservoir is equilibrated at the target pressure and temperature for 3 ns, while the kerogen entrance is kept closed using a sheet of atoms at the entrance with an artificial weak LJ potential between the sheet and methane. The entrance to the kerogen is then opened by removing the artificial sheet, and methane is allowed to adsorb into the kerogen sample under a constant pressure for tens to hundreds of nanoseconds (depending on the properties of the gas and sample) until adsorption reaches a steady state. Data for the variation in number of molecules as a function of time, $N(t)$ from the start of the main simulation, as well as the temperature of gas molecules inside the kerogen $T(t)$, are measured.

Interfacial sorption kinetics model

Recent work^{16,39} have shown that the steady transport process of hydrocarbons and carbon dioxide within nanopores is diffusion-based. From this finding, here we derive a model that best describes our set-up in Figure 1a by solving the one-dimensional diffusion equation in a single straight nanopore,⁴⁰ and extend this to a general porous network, which is given by:

$$N(t) = \Delta N \left[\frac{2}{\pi^2} \sum_{n=0}^{\infty} \frac{\exp\left(-\left(n + \frac{1}{2}\right)^2 \frac{4t}{\lambda_0 L^2}\right)}{\left(n + \frac{1}{2}\right)^2} \right] + \bar{N}, \quad (1)$$

where $\Delta N = (N_0 - \bar{N})$ is the change in the number of adsorbed gas molecules at time $t = 0$ (given by N_0) and the steady-state (given by \bar{N} , $t \rightarrow \infty$), L is the length of the kerogen sample in the direction of adsorption. Note $N_0 = 0$ in all the adsorption cases we present in the manuscript. See SI for full derivation.

The time constant τ of this adsorption process, and the ensuing scaling law, is given by an L^2 dependence:

$$\tau = \lambda_0 L^2, \quad (2)$$

where λ_0 represents the intrinsic properties of the kerogen/methane characteristics, which means it depends on reservoir pressure, temperature and the matrix properties.

Equation (1) is a solution of a diffusion-type equation⁴¹ and is general enough to deal

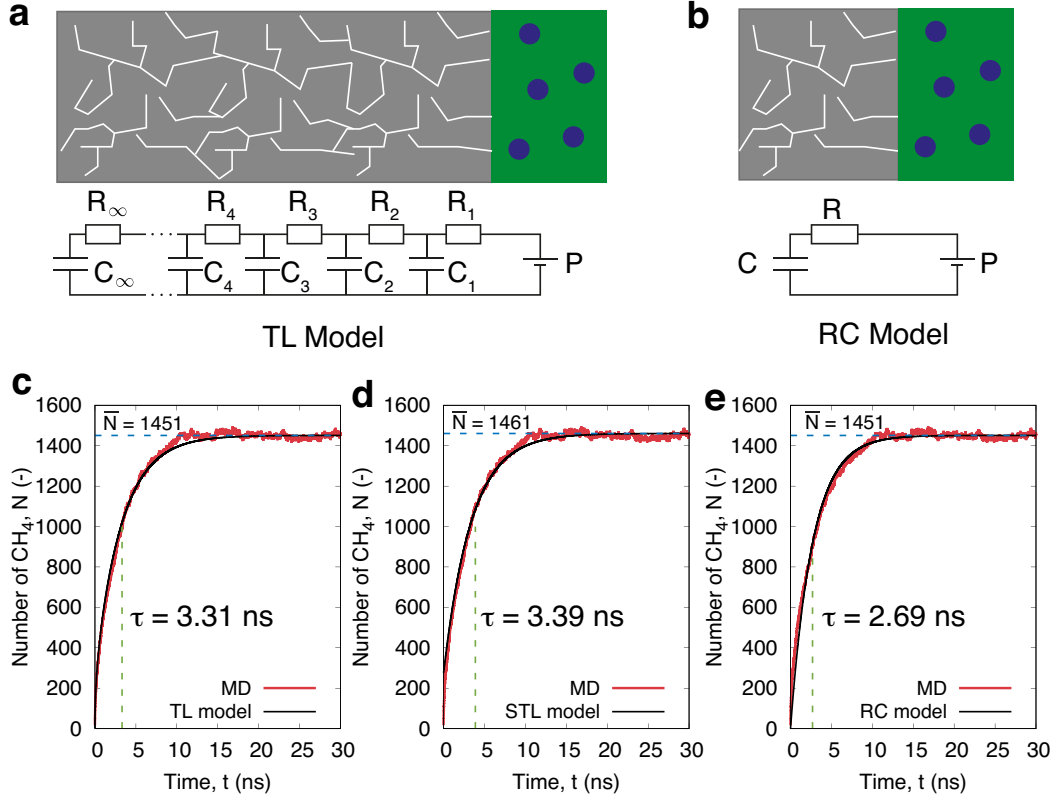


Figure 3: Schematic of the flow-equivalent electrical circuitry for (a) the TL model and (b) RC model used to describe the sorption gas kinetics in this work. MD fitting using the three kinetics models: (c) the TL model (eq. (1)), (d) the STL model (eq. (3)) and (e) the RC model (eq. (4)). The case chosen here is EFK 0.8 g/cm^3 , $P = 50 \text{ MPa}$, and kerogen length set to three times original sample, $L = 3 \times L_S$, where $L_S = 50 \text{ \AA}$ is the sample size. Horizontal and vertical dashed lines indicate the fitted value for \bar{N} and τ , respectively, using each model. Note, τ represents $\sim 63\%$ of the steady-state adsorption value, where steady-state is normally achieved at $\sim 6 \times \tau$.

with heterogeneity, meaning we can apply it to porous rock set-ups, such as ours. The expression also has analogy with the circuit of the transmission line (TL) model in electricity, which means that we can contrast the adsorption/desorption processes of methane molecules in kerogen with the charging/discharging of electrons in an electrode. As illustrated in Figure 3a, an infinite network of resistors and capacitors connected in this way can be used to describe this process, where the resistor represents the local resistance to methane flow and the capacitor is the differential capacity of local adsorption. For ease of reference, we will call equation (1) the TL model. By setting $n = 100$ terms arbitrarily, we find the TL model fits our MD data well, as we show for a random case in Figure 3c.

Theoretical model for τ

The TL model presented in the previous section in combination with the MD data we present in the results section is found to be a sufficient way of accounting for gas transport at boundary interfaces of kerogen with the larger reservoir pores. However, to verify independently our MD results, as well as provide a way of guiding future experimental measurements, in this section we propose a simplified theoretical model to estimate the adsorption time constant τ .

By inspecting equation (1), we find that ad-dends decrease exponentially with increasing n , and the first exponential governs the major sorption characteristics in our cases. Therefore, it is a reasonable assumption to keep just one term in equation (1) (i.e. setting $n = 0$), to obtain, what we call the *simplified transmission line* (STL) model:

$$N(t) = \Delta N \frac{8}{\pi^2} e^{-t/\tau} + \bar{N}. \quad (3)$$

A representative comparison between the TL and STL models is shown in Figures 3c,d, where the time constants τ are within 3% of each other, the final steady-state adsorption value of \bar{N} is within 1%, and disagreements in the STL fit arise only over a very short time interval at

the beginning of the simulation, because of the omitted terms in the series. We have not observed any visible differences between the TL and STL models across our data set.

Inspired from the electrical circuits origin of the TL and STL models, we find that the first-order RC model,^{42,43} which contains a resistor R and a capacitor C connected in serial, as shown schematically in Figure 3b, could also satisfactorily describe the sorption kinetics in simple systems:

$$N(t) = \Delta N e^{-t/RC} + \bar{N}, \quad (4)$$

where R is the flow resistance and C is the adsorption capacitance.

Given that the form of equation (4) looks very similar to the STL model (which we know is as accurate as the TL model) we can therefore make a calculated jump to equate the TL/STL sorption time constant with the RC model:

$$\tau \approx RC. \quad (5)$$

Note, we find that the RC model (equations (4) and (5)) produces a fit with the MD data that is visually less good, and errors are more pronounced in τ with $\sim 20\%$ when compared to the TL model, as shown in Figure 3e. We find that this 20% error is a systematic error as it remains in all samples and in the upscaling study.

The resistance and capacitor terms in equation (5) are given by (see full derivation in SI):

$$R = \frac{k_B T L^2}{m D_s V}, \quad (6)$$

and

$$C = M_\infty \frac{K_0}{(1 + K_0 P)^2}, \quad (7)$$

respectively, where k_B is the Boltzmann constant, m is the mass of one gas molecule, D_s is the gas self diffusion inside the kerogen, V is the box volume of the kerogen sample, M_∞ is the saturated mass of adsorbed gas molecules, and K_0 is the equilibrium constant (in units of inverse pressure). For the resistance term, we rely on a recent study¹⁷ that generated D_s using equilibrium MD simulations for the same

kerogen samples within the free-volume framework.¹⁶ The origin of the capacitance term, arises from the derivative of the Langmuir adsorption isotherm with respect to pressure. The derivations of both R and C terms are given in the SI.

Comparison with the scaling law (2), gives a theoretical expression for λ_0 :

$$\lambda_0 \approx \frac{k_B T M_\infty K_0}{m D_s V (1 + K_0 P)^2}. \quad (8)$$

Results and discussion

Validity of the adsorption kinetics model for upscaling

In this section we verify the upscaling characteristics of our adsorption kinetics model, which is carried out by varying the thickness of the kerogen slab $L = iL_s$, where i are the number of unit-cell kerogen replicas and $L_s = 50 \text{ \AA}$ is the unit-cell size (i.e. at $i = 1$); see schematic in Figure 4(a). With these being very computationally expensive MD simulations, we limit this detailed analysis to one kerogen sample only (EFK 0.8 g/cm³) until $i = 6$, but checks have been made on all other samples until $i = 3$ (see results in next section). Figure 4 summarises the key results.

Figure 4(b) shows that the fits using the TL model look visually good when compared with the MD results. Figure 4(c) verifies that steady-state adsorption is linearly proportional to L , and so there are no finite-size effects in our simulations. Figure 4(d) shows the MD data for the kerogen/gas-dependent constant λ_0 (equation (2)). We find that the value of λ_0 is roughly constant across all pressures for samples as small as $i = 2$. However, for the $i = 1$ sample, we observe deviations of λ_0 above (or below) the mean horizontal line. Similar observations are seen in all the other samples. We believe this is due to the statistical noise when fitting for τ , which is resolved by increasing the length L . Further improvements to noise reduction could be made in the future by increasing copies of the kerogen in the y/z directions, albeit at a large computational cost. Figure 4e verifies the

L^2 dependence scaling law in equation (2).

Adsorption time-scales of different kerogen porosities and maturities

In this section, we show our MD results for the adsorption time constant for all kerogen samples (of varying porosity and maturity) at fixed temperature ($T = 423 \text{ K}$). We include results for three kerogen thicknesses ($i = 1, 2, 3$), but those for $i = 2$ and $i = 3$ are scaled to $i = 1$, using equation (2), since it is the most fundamental unit cell considered. This also has the advantage of demonstrating that our results are size independent for $i \geq 2$. The TL model (equation (1)) is used only to obtain τ from the MD. We then compare these results with the theoretical model $\tau \approx RC$. Figures 5-7 show the key results of the full data set of kerogen samples and pressures.

Figure 5 shows the adsorption time constant τ measurements for the six kerogen samples we considered in order of increasing porosity, while Figure 6 shows the *estimated* resistances R . Note that we are not able to measure R in our MD simulations due to the prohibitive computational cost (see details in SI). Instead we calculate these from the relationship $R \approx \tau/C$, using knowledge of both τ (taken from the TL model fit; Fig. 5) and C (from the Langmuir fit; Fig. 7). The results for R are presented here for completeness, although they require more rigorous testing using independent transport simulations, in particular to verify the larger pressures. In the SI, we carry out basic checks using independent MD transport simulations for one kerogen sample and low pressures and verify that the R 's we are getting using this approach are close, and also match well with the theoretical values of R . Finally, it is worth stressing that the theoretical R 's (solid lines in Fig. 6) are independently calculated using equation (6).

The results in Figure 5 reveal that adsorption is faster with an increase in ϕ at most pressures, despite there being more molecules to adsorb. For example, comparing a 10% reduction in porosity between EFK08 and EFK10, we see that \bar{N} (Figure 7a) and C (Figure 7b) are always larger for EFK08 at any pressure,

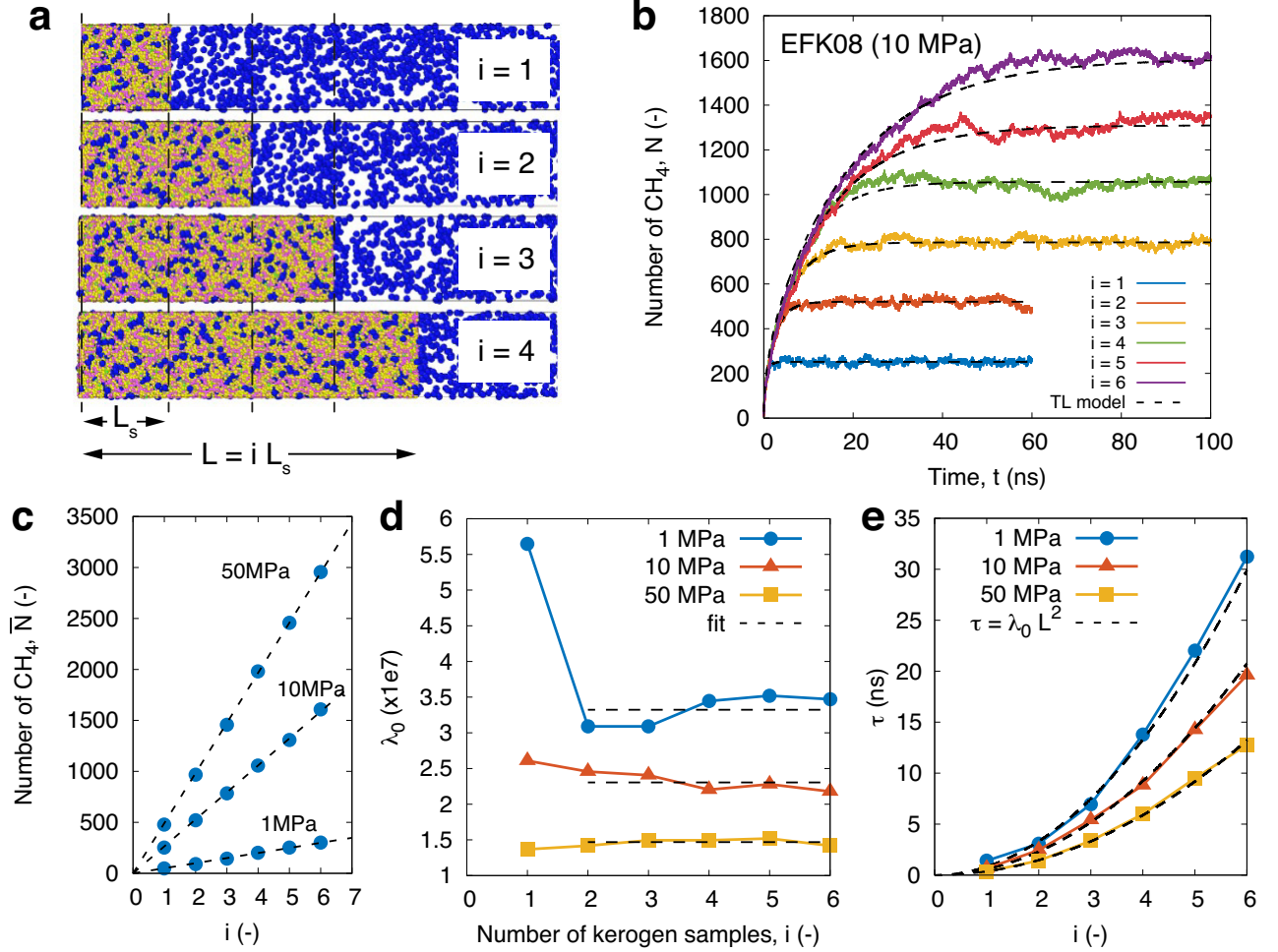


Figure 4: (a) Schematic of MD simulations with increasing kerogen thickness $L = iL_s$, where $i=1-6$ and $L_s = 50 \text{ Å}$. (b) MD data for $N(t)$ for EFK 0.8 g/cm³ (EFK08) kerogen with different lengths ($L = 50 - 300 \text{ Å}$) and $P = 10 \text{ MPa}$. MD data (coloured lines) are fitted using the TL model (equation (1); dashed black lines). (c) Steady state measurements of \bar{N} . (d) MD data for $\lambda_0 = \tau/L^2$, with horizontal fits from $i \geq 2$. (e) The adsorption time constant versus kerogen thickness for three pressures, showing the corresponding agreement of equation (2). Values for λ_0 are taken from fits from figure (d).

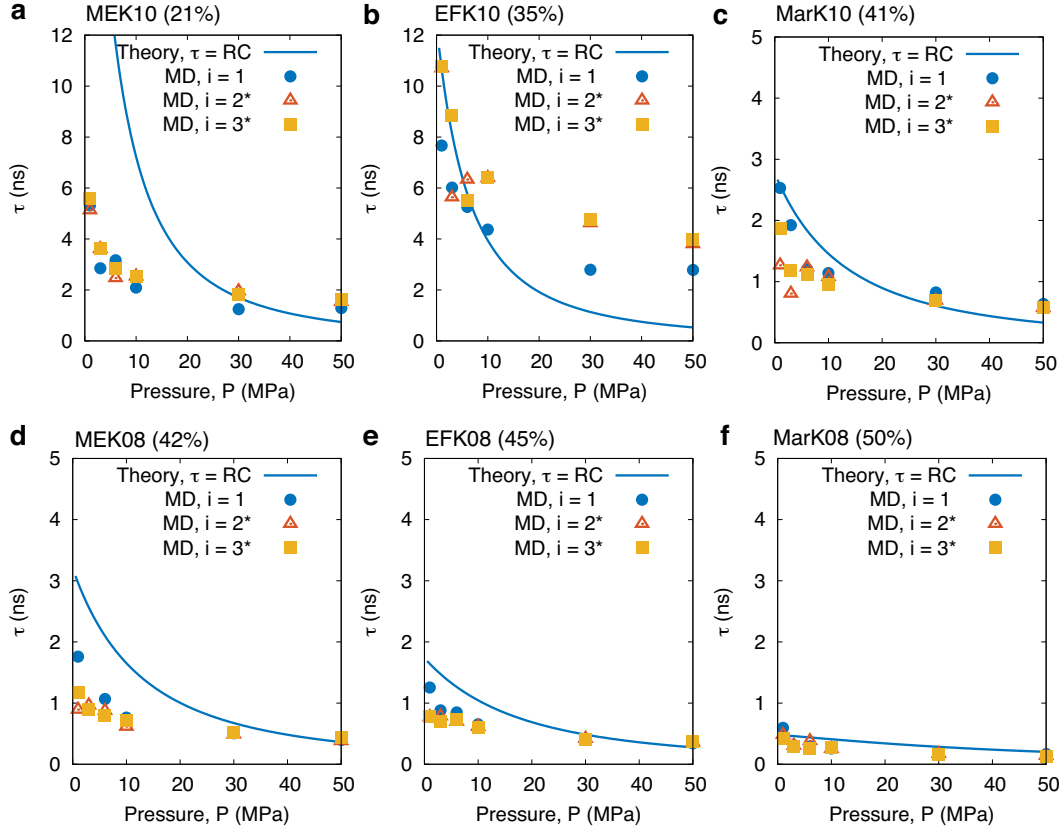


Figure 5: The effect of porosity (at $T = 423$ K) on the interfacial adsorption time constant for all samples in order of increasing porosity: (a) MEK10 ($\phi = 21\%$), (b) EFK10 ($\phi = 35\%$), (c) MarK10 ($\phi = 41\%$), (d) MEK08 ($\phi = 42\%$), (e) EFK08 ($\phi = 45\%$), (f) MarK08 ($\phi = 50\%$). Symbols are our MD results, fitted using the TL model. *We add data from thicker samples $i = 2$ and $i = 3$, but rescale them to $i = 1$ using the scaling law, equation (2). Solid lines are predictions from the theoretical model given in equation (5).

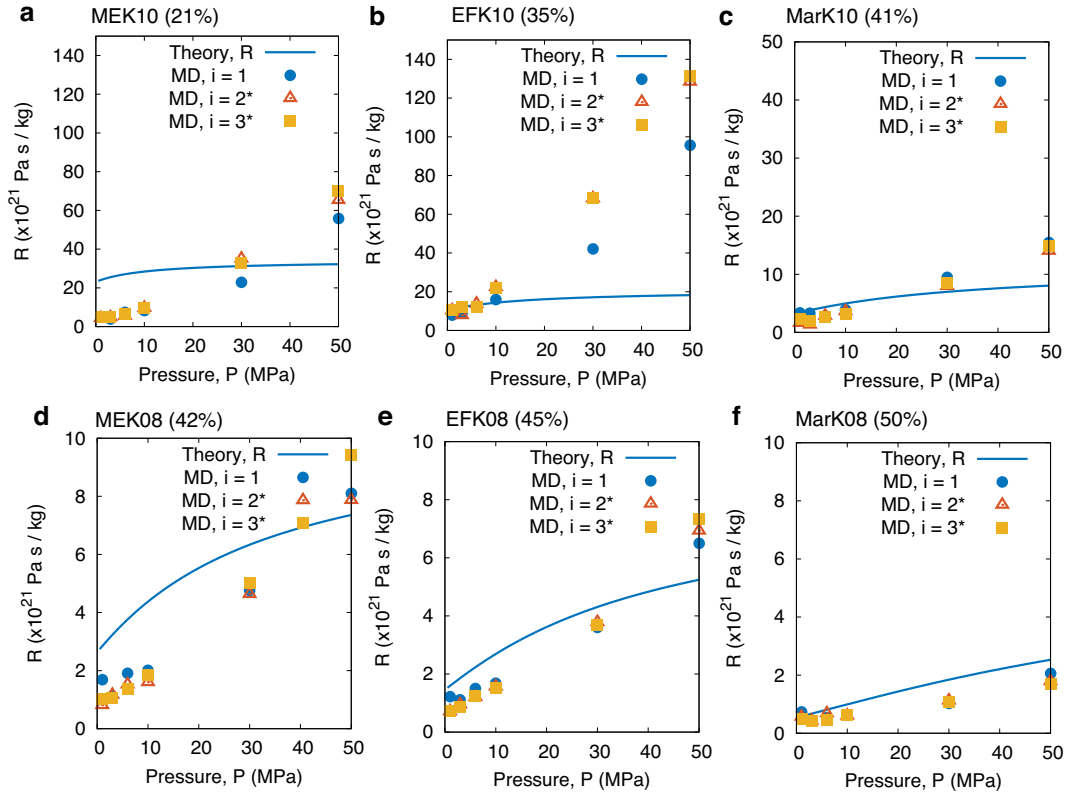


Figure 6: The effect of porosity (at $T = 423$ K) on the estimated total flow resistance R for all samples in order of increasing porosity: (a) MEK10 ($\phi = 21\%$), (b) EFK10 ($\phi = 35\%$), (c) MarK10 ($\phi = 41\%$), (d) MEK08 ($\phi = 42\%$), (e) EFK08 ($\phi = 45\%$), (f) MarK08 ($\phi = 50\%$). Symbols are our MD results, using $R \approx \tau/C$, where C and τ are obtained from Figures 7 and 5 respectively. *We add data from thicker samples $i = 2$ and $i = 3$, but rescale them to $i = 1$ using the scaling law, equation (2). Solid lines are predictions from the theoretical model given in equation (6).

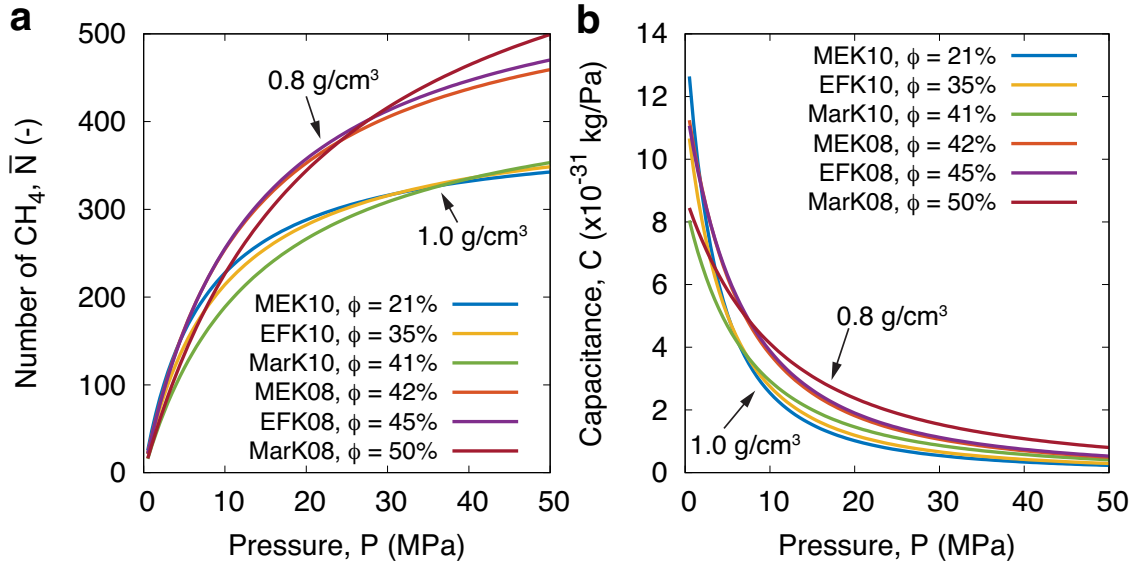


Figure 7: The effect of porosity (at $T = 423$ K) on (a) the steady-state number of adsorbed methane (Langmuir fits are shown only) and (b) kerogen capacitance (equation (7)) for all kerogen samples considered in this work.

by $\sim 50\%$ or less. However, R for EFK10 is at least one order of magnitude larger than EFK08. This proves that the kerogen’s flow resistance R (and so the self-diffusion coefficient) is the responsible factor that drives the increase in τ when porosity decreases and the pressure remains constant, rather than from the slight drop in adsorption capacitance C (see Figure 7b; purple vs yellow curves). The contribution of the adsorption capacitance C to the decrease in τ becomes more prominent for each individual kerogen sample in the case when pressure increases, since R is seen to increase with P , while both τ and C decrease with P (see Figures 5-7). Note that C represents the ability of the kerogen to store further gas molecules from a small increase in pressure, which becomes saturated as P increases.

Although kerogen samples with low porosity have a smaller accessible volume for adsorbing methane molecules, in some cases (e.g. MEK10 and EFK10) both \bar{N} and C start high at low pressures for low porous samples, as shown in Figures 7a,b. This occurs due to the strong adsorption capacitance of small pores at low pressure, as we find in our recent study.⁴⁴ As the pressure increases, however, the small pores are quickly filled, and the adsorption capacitance is then dictated by the physical accessible pore volume. At higher pressures, the high porosity kerogen samples adsorb more methane molecules and this reflects in both the Langmuir isotherms as well as the adsorption capacitance curves (Figures 7a,b).

Across our data set, the comparison between the theoretical model for τ , (solid lines in Figures 5 and 6) and our MD results are of the same order of magnitude and show similar trends with pressure and porosity, although we note there are some quantitative differences at some points. Minor checks have been made on MEK10 and EFK10 samples, where some large disagreements in R are observed. We find that EFK10 has a large anisotropy effect, where transport through one face of the sample is much slower than the other two, yet we can only currently use the full-dimension self-diffusion coefficient in the theoretical model for τ . No anisotropy is found in the other samples.

MEK10 has very minor connectivity discrepancies, and this is not surprising since its porosity is lower than the minimum percolation threshold of 23%.¹⁷

Given the historical challenges of predicting the transport in complex nano-confined flow networks, the theoretical model does a decent job. The discrepancies are also not unusual, given that ultra-tight pores, even in very simple pipe/planar geometries, are also difficult to get a perfect agreement with theoretical results for transport or self-diffusion.^{30,45}

The theoretical model we choose for $\tau \approx RC$, as well as the use of steady-state models for R and C to predict transient solutions, are assumptions that need challenging in the future, even though we have calibrated each term using independent but representative MD data of the same kerogen and gas combination. For example, one suggestion would be that the values for self-diffusion taken from Obliger et. al¹⁷ for rigid samples, on which our R depends, could be carefully rechecked and recalibrated for a flexible matrix. Further improvements could be made by understanding how to incorporate the effect of non-linearities arising from R and C with pressure, and getting further inspiration from electrical circuit theory to improve the theoretical model.

Conclusions

Non-equilibrium molecular dynamics simulations are used to measure the time-varying adsorption of methane in organic tight porous rock, known as kerogen. We propose a sorption kinetics model that is able to capture the time-variation of the gas inside kerogen with the MD very well. The sorption kinetics model has also allowed us to rationalise the process using the adsorption time constant τ , which we do for all pressures relevant to shale, and various samples from different geological conditions (fields, maturities, porosities). Our results show there is a clear correlation between porosity, pressure and τ : higher pressures and higher porosities have faster adsorption time scales. We attribute this to a decrease in flow resistance R (higher dif-

fusion) of methane inside the matrix, despite having a higher adsorption capacitance C for larger porosities. However, we also show that the adsorption capacitance is important when pressure is varied for single kerogen samples, since τ and C both drop with pressure, as R increases. This arises from the non-linear profile of the adsorption isotherm at higher pressures. In this analysis, we have adopted an approximate theoretical model for τ , which is inspired from electrical circuitry. This model gave good qualitative agreement with our results, but may need to be refined further for better predictive accuracy. The theoretical model for τ could also be used to guide future experiments.

This work now provides a route to implement new flux boundary conditions that model the time-varying sorption processes in higher scale flow models, where the TL model and the calibration of MD data presented can be used. Advanced flow models^{28–31} currently being developed to model the three-dimensional low-speed, rarefied-to-dense gas flows inside shale rock are currently missing these types of boundary models. Therefore simulations showing the effect of time-varying adsorption/desorption processes near kerogen boundaries, on the transport inside the larger meso/macro pores can now be studied. This work also produces a protocol for studying the behaviour of other gases or liquids in shale that are becoming important for stimulation, as well as reservoir gas storage schemes, such as for carbon dioxide sequestration or hydrogen energy storage.

Acknowledgement The authors would like to thank Colin Bousige (and co workers) for providing us the kerogen structures used in this work. This work was financial supported by King Fahd University of Petroleum and Minerals (KFUPM), Saudi Arabia. All MD simulations were run on ARCHER2, the UK’s national supercomputing service. MKB and LG thank support from the Engineering and Physical Sciences Research Council (EP/N016602/1, EP/R007438/1 and EP/V012002/1). For the purpose of open access, the author has applied a CC BY public copyright licence to any Author Accepted Manuscript version arising from

this submission.

Supporting Information Available

A Supporting Information (SI) document is available that includes the following:

- Assessment of rigid vs thermal modelling of kerogen atoms on the adsorption kinetics;
- Derivations of the interfacial sorption kinetics model and the adsorption time constant model;
- Validation study of the transport model in kerogen;
- Generated MD adsorption data.

Sample LAMMPS files and the raw MD adsorption simulation data are available open access at: <https://doi.org/10.7488/ds/3805>.

References

- (1) Yuan, J.; Luo, D.; Feng, L. A review of the technical and economic evaluation techniques for shale gas development. *Appl. Energy* **2015**, *148*, 49–65.
- (2) Gensterblum, Y.; Ghanizadeh, A.; Cuss, R. J.; Amann-Hildenbrand, A.; Krooss, B. M.; Clarkson, C. R.; Harrington, J. F.; Zoback, M. D. Gas transport and storage capacity in shale gas reservoirs—A review. Part A: Transport processes. *J. Unconv. Oil Gas Resour.* **2015**, *12*, 87–122.
- (3) Chen, C.; Hu, W.; Sun, J.; Li, W.; Song, Y. CH₄ adsorption and diffusion in shale pores from molecular simulation and a model for CH₄ adsorption in shale matrix. *Int. J. Heat Mass Transf.* **2019**, *141*, 367–378.
- (4) Curtis, J. B. Fractured Shale-Gas Systems. *AAPG Bulletin* **2002**, *86*, 1921–1938.

- (5) Rexer, T. F.; Mathia, E. J.; Aplin, A. C.; Thomas, K. M. High-Pressure Methane Adsorption and Characterization of Pores in Posidonia Shales and Isolated Kerogens. *Energy Fuels* **2014**, *28*, 2886–2901.
- (6) Bowker, K. A. Barnett Shale gas production, Fort Worth Basin: Issues and discussion. *AAPG Bulletin* **2007**, *91*, 523–533.
- (7) Yethiraj, A.; Striolo, A. Fracking: What Can Physical Chemistry Offer? *J. Phys. Chem. Lett.* **2013**, *4*, 687–690.
- (8) Cueto-Felgueroso, L.; Juanes, R. Forecasting long-term gas production from shale. *PNAS* **2013**, *110*, 19660–19661.
- (9) Busch, A.; Gensterblum, Y.; Krooss, B. M.; Littke, R. Methane and carbon dioxide adsorption–diffusion experiments on coal: upscaling and modeling. *Int. J. Coal Geol.* **2004**, *60*, 151–168.
- (10) Yucel Akkutlu, I.; Fathi, E. Multiscale Gas Transport in Shales With Local Kerogen Heterogeneities. *SPE J* **2012**, *17*, 1002–1011.
- (11) Etminan, S. R.; Javadpour, F.; Maini, B. B.; Chen, Z. Measurement of gas storage processes in shale and of the molecular diffusion coefficient in kerogen. *Int. J. Coal Geol.* **2014**, *123*, 10–19.
- (12) Chen, L.; Zuo, L.; Jiang, Z.; Jiang, S.; Liu, K.; Tan, J.; Zhang, L. Mechanisms of shale gas adsorption: Evidence from thermodynamics and kinetics study of methane adsorption on shale. *Chem. Eng. J.* **2019**, *361*, 559–570.
- (13) Ruckenstein, E.; Vaidyanathan, A.; Youngquist, G. Sorption by solids with bidisperse pore structures. *Chem. Eng. Sci.* **1971**, *26*, 1305–1318.
- (14) Yuan, W.; Pan, Z.; Li, X.; Yang, Y.; Zhao, C.; Connell, L. D.; Li, S.; He, J. Experimental study and modelling of methane adsorption and diffusion in shale. *Fuel* **2014**, *117*, 509–519.
- (15) Clarkson, C.; Bustin, R. The effect of pore structure and gas pressure upon the transport properties of coal: a laboratory and modeling study. 2. Adsorption rate modeling. *Fuel* **1999**, *78*, 1345–1362.
- (16) Falk, K.; Coasne, B.; Pellenq, R.; Ulm, F.-J.; Bocquet, L. Subcontinuum mass transport of condensed hydrocarbons in nanoporous media. *Nat. Commun.* **2015**, *6*, 1–7.
- (17) Obliger, A.; Ulm, F. J.; Pellenq, R. Impact of Nanoporosity on Hydrocarbon Transport in Shales’ Organic Matter. *Nano Lett.* **2018**, *18*, 832–837.
- (18) Akilu, S.; Padmanabhan, E.; Sun, Z. A review of transport mechanisms and models for unconventional tight shale gas reservoir systems. *Int. J. Heat Mass Transf.* **2021**, *175*, 121125.
- (19) Gensterblum, Y.; Ghanizadeh, A.; Cuss, R. J.; Amann-Hildenbrand, A.; Krooss, B. M.; Clarkson, C. R.; Harrington, J. F.; Zoback, M. D. Gas transport and storage capacity in shale gas reservoirs – A review. Part A: Transport processes. *J. Unconv. Oil Gas Resour.* **2015**, *12*, 87–122.
- (20) Shan, B.; Wang, R.; Guo, Z.; Wang, P. Contribution quantification of nanoscale gas transport in shale based on strongly inhomogeneous kinetic model. *Energy* **2021**, *228*, 120545.
- (21) Shan, B.; Wang, P.; Wang, R.; Zhang, Y.; Guo, Z. Molecular kinetic modelling of nanoscale slip flow using a continuum approach. *J. Fluid Mech.* **2022**, *939*.
- (22) Yu, H.; Chen, J.; Zhu, Y.; Wang, F.; Wu, H. Multiscale transport mechanism of shale gas in micro/nano-pores. *Int. J. Heat Mass Transf.* **2017**, *111*, 1172–1180.

- (23) Wu, H.; Chen, J.; Liu, H. Molecular dynamics simulations about adsorption and displacement of methane in carbon nanochannels. *J. Phys. Chem. C* **2015**, *119*, 13652–13657.
- (24) Yuan, Q.; Zhu, X.; Lin, K.; Zhao, Y.-P. Molecular dynamics simulations of the enhanced recovery of confined methane with carbon dioxide. *Phys. Chem. Chem. Phys.* **2015**, *17*, 31887–31893.
- (25) Liu, J.; Xie, H.; Wang, Q.; Chen, S.; Hu, Z. Influence of pore structure on shale gas recovery with CO₂ sequestration: insight into molecular mechanisms. *Energy Fuels* **2019**, *34*, 1240–1250.
- (26) Rezlerová, E.; Brennan, J. K.; Lísál, M. Methane and carbon dioxide in dual-porosity organic matter: Molecular simulations of adsorption and diffusion. *AIChE J.* **2021**, *67*, e16655.
- (27) Rezlerová, E.; Jain, S. K.; Lísál, M. Adsorption, Diffusion, and Transport of C₁ to C₃ Alkanes and Carbon Dioxide in Dual-Porosity Kerogens: Insights from Molecular Simulations. *Energy Fuels* **2023**, *37*, 492–508.
- (28) Ho, M. T.; Zhu, L.; Wu, L.; Wang, P.; Guo, Z.; Li, Z.-H.; Zhang, Y. A multi-level parallel solver for rarefied gas flows in porous media. *Comput. Phys. Commun.* **2019**, *234*, 14–25.
- (29) Ho, M. T.; Li, J.; Wu, L.; Reese, J. M.; Zhang, Y. A comparative study of the DSBGK and DVM methods for low-speed rarefied gas flows. *Comput. Fluids* **2019**, *181*, 143–159.
- (30) Corral-Casas, C.; Gibelli, L.; Borg, M. K.; Li, J.; Al-Afnan, S. F. K.; Zhang, Y. Self-diffusivity of dense confined fluids. *Phys. Fluids* **2021**, *33*, 082009.
- (31) Li, J.; Ho, M. T.; Borg, M. K.; Cai, C.; Li, Z.-H.; Zhang, Y. Pore-scale gas flow simulations by the DSBGK and DVM methods. *Comput. Fluids* **2021**, *226*, 105017.
- (32) Bousige, C.; Ghimbeu, C. M.; Vix-Guterl, C.; Pomerantz, A. E.; Suleimenova, A.; Vaughan, G.; Garbarino, G.; Feynson, M.; Wildgruber, C.; Ulm, F.-J.; Pellenq, R. J. M.; Coasne, B. Realistic molecular model of kerogen's nanostructure. *Nat. Mater.* **2016**, *15*, 576–582.
- (33) Martin, M. G.; Siepmann, J. I. Transferable potentials for phase equilibria. 1. United-atom description of n-alkanes. *J. Phys. Chem. B* **1998**, *102*, 2569–2577.
- (34) Plimpton, S. Fast parallel algorithms for short-range molecular dynamics. *J. Comput. Phys.* **1995**, *117*, 1–19.
- (35) Evans, D. J.; Holian, B. L. The Nose–Hoover thermostat. *J. Chem. Phys.* **1985**, *83*, 4069–4074.
- (36) Wu, T.; Firoozabadi, A. Effect of Microstructural Flexibility on Methane Flow in Kerogen Matrix by Molecular Dynamics Simulations. *J. Phys. Chem. C* **2019**, *123*, 10874–10880.
- (37) Obliger, A.; Valdenaire, P.-L.; Ulm, F.-J.; Pellenq, R. J.-M.; Leyssale, J.-M. Methane diffusion in a flexible kerogen matrix. *J. Phys. Chem. B* **2019**, *123*, 5635–5640.
- (38) Linstrom, P.; Mallard, W. NIST Chemistry WebBook, NIST Standard Reference Database Number 69, National Institute of Standards and Technology, Gaithersburg MD, 20899, <http://webbook.nist.gov>. 2022.
- (39) Moh, D. Y.; Zhang, H.; Wang, S.; Yin, X.; Qiao, R. Soaking in CO₂ huff-n-puff: A single-nanopore scale study. *Fuel* **2022**, *308*, 122026.
- (40) Wang, R.; Bi, S.; Guo, Z.; Feng, G. Molecular insight into replacement dynamics of CO₂ enhanced oil recovery in nanopores. *Chem. Eng. J.* **2022**, *440*, 135796.

- (41) Kornyshev, A. A.; Twidale, R. M.; Kolomeisky, A. B. Current-generating double-layer shoe with a porous sole: ion transport matters. *J. Phys. Chem. C* **2017**, *121*, 7584–7595.
- (42) Péan, C.; Merlet, C.; Rotenberg, B.; Madden, P. A.; Taberna, P.-L.; Daffos, B.; Salanne, M.; Simon, P. On the Dynamics of Charging in Nanoporous Carbon-Based Supercapacitors. *ACS Nano* **2014**, *8*, 1576–1583.
- (43) Péan, C.; Rotenberg, B.; Simon, P.; Salanne, M. Multi-scale modelling of supercapacitors: From molecular simulations to a transmission line model. *J. Power Sources* **2016**, *326*, 680–685.
- (44) Wang, R.; Li, J.; Gibelli, L.; Guo, Z.; Borg, M. K. Sub-nanometre pore adsorption of methane in kerogen. *Chem. Eng. J.* **2021**, *426*, 130984.
- (45) Wu, L.; Liu, H.; Reese, J. M.; Zhang, Y. Non-equilibrium dynamics of dense gas under tight confinement. *J. Fluid Mech.* **2016**, *794*, 252–266.